

Tunneling current modulation in atomically precise graphene nanoribbon heterojunctions

Boris Senkovskiy (✉ senkovskiy@gmail.com)

University of Cologne <https://orcid.org/0000-0003-1443-6780>

Alexey Nenashev

Novosibirsk State University <https://orcid.org/0000-0002-1022-0731>

Seyed Alavi

University of Cologne

Yannic Falke

University of Cologne

Martin Hell

University of Cologne

Pantelis Bampoulis

University of Cologne

Dimitry Rybkovskiy

Prokhorov General Physics Institute

Dmitry Usachov

Saint Petersburg State University

Alexander Fedorov

Leibniz Institute for Solid State and Materials Research

Alexander Chernov

University of Cologne

Florian Gebhard

Philipp University of Marburg

Klaus Meerholz

University of Cologne

Dirk Hertel

University of Cologne <https://orcid.org/0000-0002-0421-9734>

Masashi Arita

Hiroshima University

Taichi Okuda

Hiroshima Synchrotron Radiation Center, Hiroshima University <https://orcid.org/0000-0002-5790-3847>

Koji Miyamoto

Hiroshima Synchrotron Radiation Center, Hiroshima University

Kenya Shimada

Hiroshima University <https://orcid.org/0000-0002-1945-2352>

Felix Fischer

University of California, Berkeley

Thomas Michely

University Cologne

Sergei Baranovskii

Philipp University of Marburg

Klas Lindfors

University of Cologne

Thomas Szkopek

McGill University <https://orcid.org/0000-0003-1152-6043>

Alexander Grueneis

University of Cologne <https://orcid.org/0000-0003-2448-6060>

Article

Keywords: GNRs, spectroscopic properties, charge transport, scanning tunneling microscopy, angle-resolved photoemission, Raman spectroscopy, charge transport

Posted Date: September 16th, 2020

DOI: <https://doi.org/10.21203/rs.3.rs-74344/v1>

License:  This work is licensed under a Creative Commons Attribution 4.0 International License.

[Read Full License](#)

Version of Record: A version of this preprint was published at Nature Communications on May 5th, 2021.

See the published version at <https://doi.org/10.1038/s41467-021-22774-0>.

Tunneling current modulation in atomically precise graphene nanoribbon heterojunctions

Boris V. Senkovskiy¹, Alexey V. Nenashev^{2,3}, Seyed K. Alavi^{4,5}, Yannic Falke¹, Martin Hell¹, Pantelis Bampoulis¹, Dmitry V. Rybkovskiy⁶, Dmitry Yu. Usachov⁷, Alexander V. Fedorov⁸, Alexander I. Chernov^{1,9,10}, Florian Gebhard¹¹, Klaus Meerholz⁴, Dirk Hertel⁴, Masashi Arita¹², Taichi Okuda¹², Koji Miyamoto¹², Kenya Shimada¹², Felix R. Fischer^{13,14,15}, Thomas Michely¹, Sergei D. Baranovskii¹¹, Klas Lindfors⁴, Thomas Szkopek¹⁶, Alexander Grüneis¹

¹*II. Physikalisches Institut, Universität zu Köln, Zùlpicher Strasse 77, 50937 Köln, Germany*

²*Rzhanov Institute of Semiconductor Physics, 630090 Novosibirsk, Russia*

³*Department of Physics, Novosibirsk State University, 630090 Novosibirsk, Russia*

⁴*Department für Chemie, Universität zu Köln, Greinstrasse 4-6, 50939 Köln, Germany*

⁵*Institut für Angewandte Physik der Universität Bonn, Wegeler Strasse 8, 53115 Bonn, Germany*

⁶*Skolkovo Institute of Science and Technology, Skolkovo Innovation Center 121025, 3 Nobel Street, Moscow, Russia*

⁷*Saint Petersburg State University, Uljanovskaya 1, Saint Petersburg 198504, Russia*

⁸*IFW Dresden, P.O. Box 270116, Dresden D-01171, Germany*

⁹*Moscow Institute of Physics and Technology (State University), 141700, Dolgoprudny, Russia*

¹⁰*Russian Quantum Center, Skolkovo innovation city, 121205, Moscow, Russia*

¹¹*Faculty of Physics and Material Sciences Center, Philipps-Universität, D-35032 Marburg, Germany*

¹²*Hiroshima Synchrotron Radiation Center, Hiroshima University, 739-0046, Japan*

¹³*Department of Chemistry, University of California at Berkeley, Tan Hall 680, Berkeley, CA 94720, USA*

¹⁴*Materials Sciences Division, Lawrence Berkeley National Laboratory, Berkeley, CA 94720, USA*

¹⁵*Kavli Energy NanoSciences Institute at the University of California Berkeley and the Lawrence Berkeley National Laboratory, Berkeley, California 94720, USA*

¹⁶*McGill University, Department of Electrical and Computer Engineering, H3A 2A7, Canada*

Lateral heterojunctions of atomically precise graphene nanoribbons (GNRs) hold promise for applications in nanotechnology, yet their charge transport and most of the spectroscopic properties have not been investigated. Here, we synthesize a monolayer of multiple aligned heterojunctions consisting of quasi-metallic and wide-bandgap GNRs, and report characterization by scanning tunneling microscopy, angle-resolved photoemission, Raman spectroscopy, and charge transport. Comprehensive transport measurements as a function of bias and gate voltages, channel length, and temperature reveal that charge transport is dictated by tunneling through the potential barriers formed by wide-bandgap GNR segments. The current-voltage characteristics are in agreement with calculations of tunneling conductance through asymmetric barriers. We fabricate a GNR heterojunctions based sensor and demonstrate greatly improved sensitivity to adsorbates compared to graphene based sensors. This is achieved via a new concept in sensing, namely the modulation of the tunneling barriers by adsorbates.

Introduction

The significance of heterojunctions is established in semiconductor physics. Vertically grown compound semiconductor heterostructures such as GaAs/Al_xGa_{1-x}As,^{1,2} have been developed to enable high electron mobility transistors, light-emitting diodes, laser diodes, and solar cells. Tunneling through multiple potential barriers in superlattice heterostructures^{3,4} has found use in quantum cascade lasers.⁵ More recently, van der Waals (vdW) heterostructures that are fabricated from monolayers of layered materials have attracted research interest.^{6,7} Graphene nanoribbon (GNR) heterostructures differ from compound semiconductor and vdW heterostructures in that the bottom-up synthesis allows for the formation of one-dimensional (1D) *lateral* interfaces with atomic precision. This synthesis approach enables electronic band structure engineering, i.e. control of parameters such as the energy bandgap, the band offset and the effective mass of carriers that are important for charge transport.⁸⁻¹⁵ Conventional top-down fabrication methods such as lithography do not have the precision required for reproducible, atomically precise GNR heterojunctions that have well-defined, sharp band offsets. Thus bottom-up GNR heterojunctions are promising for novel device concepts such as energy-efficient tunnel field-effect transistors (TFETs).¹⁵⁻¹⁷ TFETs based on GNR heterostructures might also be useful for chemical sensing devices. Yet progress is hampered by the absence of experiments that probe the electronic properties of GNR heterojunctions.

In the present work, we use the lateral fusion approach to fabricate a monolayer film consisting of aligned lateral heterojunctions of wide-bandgap armchair GNRs of $N=7$ carbon atom

width (7-AGNRs) and their quasi-metallic derivatives (mostly 14-AGNRs) on a stepped Au(788) surface. The GNR heterojunctions are comprehensively characterized by scanning-tunneling microscopy (STM), angle-resolved photoemission spectroscopy (ARPES) and Raman spectroscopy, and are integrated into a back-gated field effect transistor (FET) structure. We demonstrate that the current through the device has the characteristic dependencies on bias voltage, charge carrier concentration, channel length, and temperature that are associated with tunneling transport. We quantitatively describe the charge transport behaviour of GNR heterojunction devices using a multi-barrier tunneling model. Performing chemical doping of GNR heterojunctions with alkali metal adatoms, we observe a highly superlinear modulation of the tunneling current in lieu of the conventional linear current modulation. Our observations of tunneling conductance and chemical sensing using atomically precise GNR heterojunctions highlight their application potential.

GNR heterojunction concept

Fig. 1a schematically shows densely aligned, parallel 7-AGNRs such as those grown on a stepped Au(788) crystal.^{18,19} Thermally activated lateral fusion leads to the formation of narrow-bandgap 14-AGNR segments as illustrated in Fig. 1b. Charge transport can be probed by transferring such a heterojunction array to an insulating substrate and depositing metallic electrodes to form source and drain contacts. For simplicity, electrodes are sketched on top of 14-AGNRs, forming quasi-Ohmic contacts. The wide-bandgap 7-AGNR segments act as energy barriers. Charge carriers traverse a multiple barrier potential profile (Fig. 1c). There are two primary mechanisms of charge transport from one quasi-metallic 14-AGNR segment to another: tunneling through the 7-AGNR

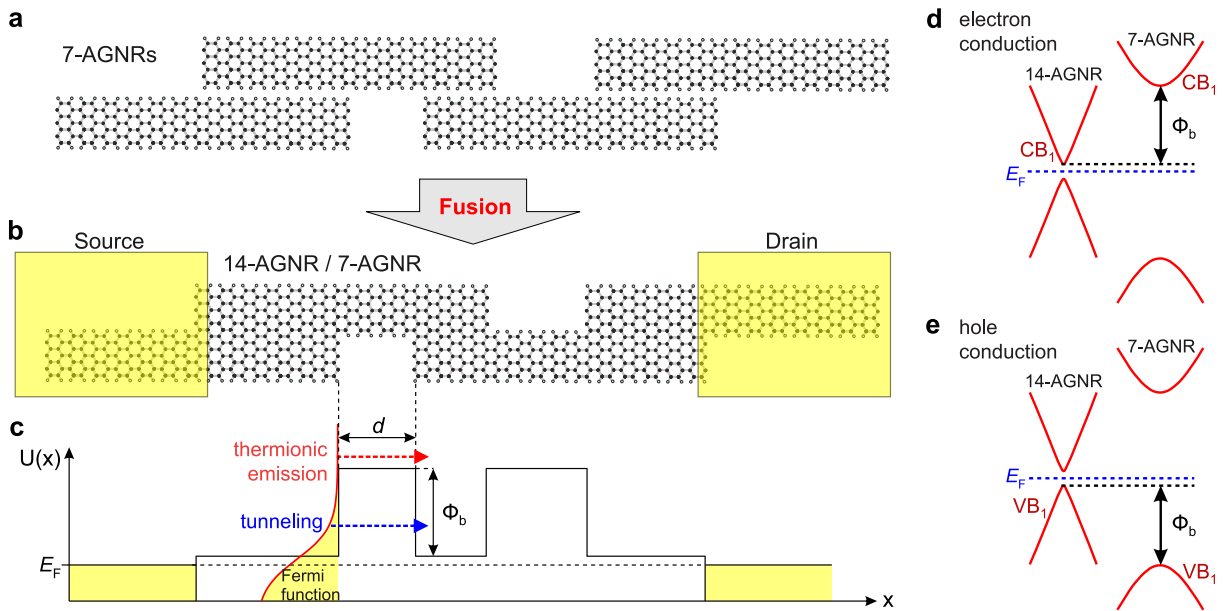


Fig. 1 Fabrication and electronic structure of GNR heterojunctions. (a, b) Schematic illustration of the lateral fusion that forms 14-AGNR segments from two adjacent 7-AGNRs. When the source-drain contacts are fabricated, the remaining 7-AGNR segments act as tunneling barriers. (c) Potential $U(x)$ as a function of coordinate x between source and drain contacts of multiple 7-/14-AGNR heterojunctions. The barrier height Φ_b and the barrier length d are indicated. Thermionic emission and tunneling mechanisms are schematically shown. (d, e) Sketch of the electronic energy band dispersions of 7-AGNR and 14-AGNR. The conduction and valence band edges are CB_1 and VB_1 , respectively, and determine the value of Φ_b .

barrier and thermionic emission over the barrier (Fig. 1c). The tunneling and thermionic currents depend on temperature (with the temperature dependence of the latter much stronger than the former), on the applied electric field, and on the barrier shape. The barrier length d is the length of the 7-AGNR segment. For electron (hole) injection from the 14-AGNR segment into the 7-AGNR segment, the barrier height Φ_b is given by the conduction (valence) band offset, i.e. the difference between the first conduction (valence) sub-bands of the 7- and 14-AGNR (Fig. 1d,e).

Synthesis and characterization of GNR heterojunctions

STM studies reveal that the lateral fusion (see Methods) of densely aligned 7-AGNRs on a Au(788) crystal leads to the formation of numerous 14-AGNRs (Fig. 2a, and Supplementary Section 1). Wider GNRs with $N = 21, 28$ and so forth are less abundant, and are also quasi-metallic, similarly to 14-AGNRs and hence will not affect our conclusions.¹² The fused GNRs have a length of the order of tens of nm, and many of them are connected by short (several nm) 7-AGNR segments. Together, these form well-aligned paths for charge transport (Fig. 2a). We characterize fused GNRs by ARPES and ultra-high vacuum (UHV) Raman spectroscopy.¹⁹ Upon fusion of aligned 7-AGNRs we observe new features in the ARPES spectra (Supplementary Section 2). A linearly dispersing energy band is observed, consistent with calculations (Figs. 2b,c and Methods). Based on the peculiar variation of the photoemission intensity for GNRs in momentum space (Supplementary Section 2), we attribute this band to the first valence sub-band of 14-AGNRs, labelled $\text{VB}_1^{14\text{-AGNR}}$ hereinafter. The apex of $\text{VB}_1^{14\text{-AGNR}}$ is touching the Fermi level (E_F), which is in line with the observed Fermi level pinning in GNRs on a Au substrate.²¹ UHV Raman spectra before

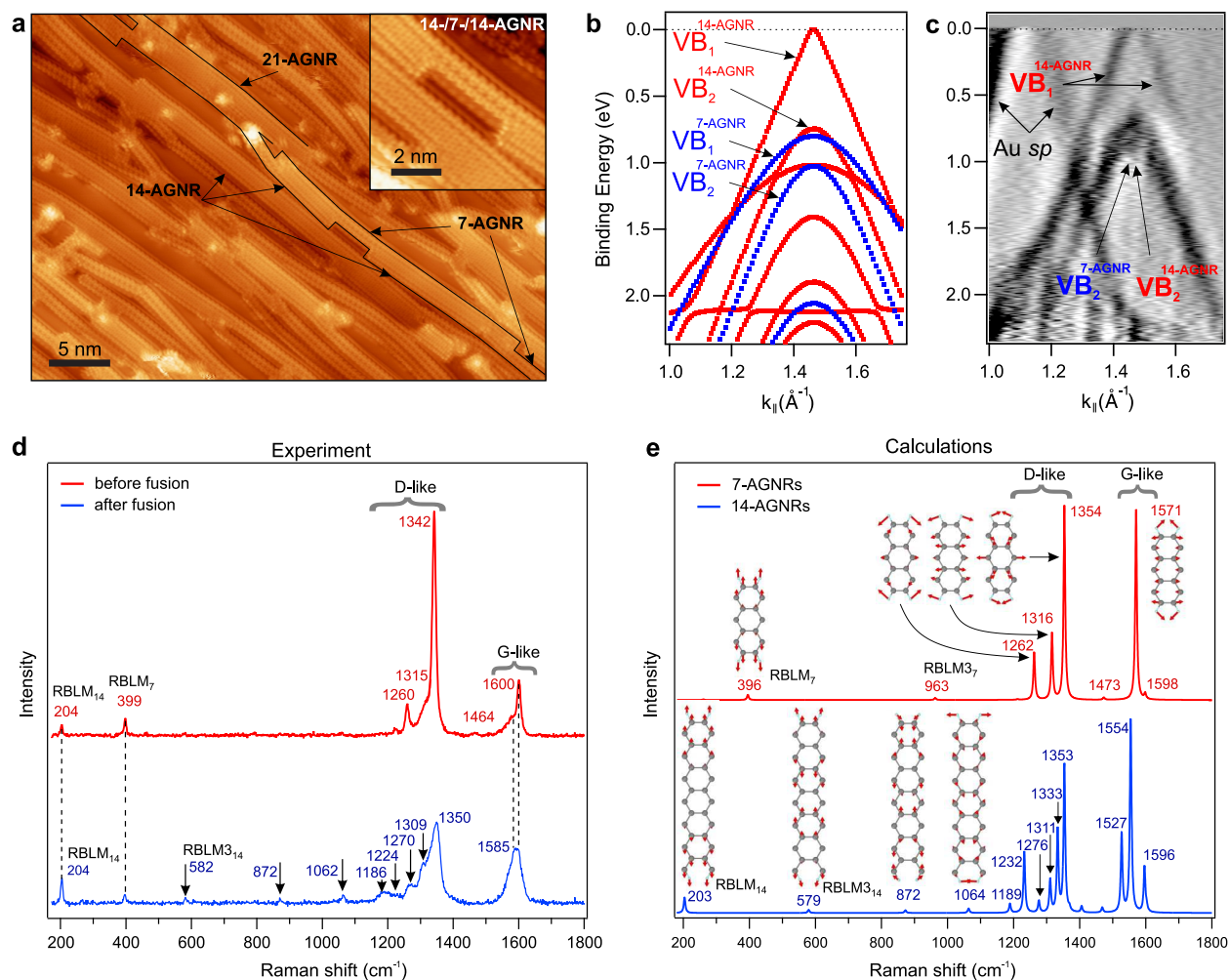


Fig. 2 Experimental characterization of GNR heterojunctions on Au(788). (a) STM topographic image of fused 7-AGNRs (sample bias $V_s = -1.3$ V, tunneling current $I_t = 1.8$ nA). The black lines outline one possible conducting path through the GNR heterojunctions: quasi-metallic 14- and 21-AGNRs connected by 7-AGNR segments. The inset shows an example of a typical 14-/7-/14-AGNR heterojunction with a short (~ 3 nm) 7-AGNR segment. See also Supplementary Section 1. (b) Calculated electronic band structure of 7-AGNRs (blue) and 14-AGNRs (red) shown in the second Brillouin zone of GNRs, where the ARPES scans were acquired. The valence band maxima in the calculations are aligned to the ARPES data. (c) Second derivative with respect to momentum of the ARPES scan (to enhance the contrast) of fused GNRs on Au(788) measured along the GNR axis (k_{\parallel}) with fixed in-plane momentum perpendicular to the axis (k_{\perp}).²⁰ To maximize the photoemission intensity from $VB_1^{14\text{-AGNR}}$, we used $k_{\perp} = 1.1 \text{ \AA}^{-1}$. At this k_{\perp} the intensities from $VB_2^{14\text{-AGNR}}$ and $VB_2^{7\text{-AGNR}}$ overlap (Supplementary Section 2). The Au *sp* bands that are from the substrate are also indicated. (d) UHV Raman spectra (300 K, 633 nm) of GNRs on Au(788) before and after fusion. The frequencies of the respective Raman peaks are indicated (values in cm^{-1}). (e) Calculated Raman spectra of 7- and 14-AGNR. Eigenvectors of selected phonon modes are shown (Supplementary Section 4). The RBLM_{3₇} and RBLM_{3₁₄} are the third overtones of RBLM₇ and RBLM₁₄, respectively.

and after the fusion were measured *in situ* (Fig. 2d) and are compared to the calculations (see Methods) for 7-AGNRs and 14-AGNRs (Fig. 2e). The initial Raman spectrum consists primarily of 7-AGNR derived modes. Upon fusion we observe changes in the regions of the G-like and D-like modes (whose atomic displacements resemble the G and D modes in graphene), and the appearance of well separated peaks in the low-frequency region. We observe radial breathing-like modes at 399 cm^{-1} for 7-AGNRs (RBLM₇) and at 204 cm^{-1} for 14-AGNRs (RBLM₁₄). The frequencies of all peaks that appear after fusion are in excellent agreement with the calculations for 14-AGNRs. During GNR fusion we have monitored the UHV Raman spectrum which allowed us to optimize the process for maximum 14-AGNR peak intensities (Supplementary Section 4). STM, ARPES and Raman spectroscopy measurements consistently show that the fused sample is a monolayer of aligned multiple heterojunctions of quasi-metallic GNRs and wide-bandgap 7-AGNR segments.

Charge transport characterization

For the transport measurements, a film of aligned GNR heterojunctions was transferred to a doped Si wafer with 300 nm SiO₂ using electrochemical delamination²² to fabricate back-gated FETs. The GNR orientation and structural quality of the transferred sample were confirmed by polarized Raman measurements (Supplementary Section 4). Electrical contacts to the film were fabricated by electron-beam lithography. In the FET devices (Fig. 3a), the drain current I_d was measured as a function of the drain voltage V_d and the back-gate voltage V_g . We fabricated devices with different channel lengths L and a fixed channel width W (25 μm). The GNR heterojunctions were aligned

along the channel between the source and drain contacts. After device fabrication, each sample was mounted on a sample holder that enables charge transport measurements to be carried out in UHV.

We observe nonlinear I_d - V_d behavior and a clear V_g dependence (Fig. 3b). A strong field effect is observed for both electron ($V_g > 0$) and hole ($V_g < 0$) conduction, demonstrating bipolar operation (Fig. 3c). The current I_d is modulated by V_g by two orders of magnitude, with higher hole conduction than electron conduction. We extract the field-effect mobility using the direct transconductance method (DTM): $\mu_{\text{DTM}} = 6.0 \times 10^{-5} \text{ cm}^2/\text{Vs}$ at $V_d = 6 \text{ V}$ and $\mu_{\text{DTM}} = 8.3 \times 10^{-4} \text{ cm}^2/\text{Vs}$ at $V_d = 9 \text{ V}$ (see Methods). Such low values of μ_{DTM} cannot be explained by conventional band transport and are more typically associated with hopping transport, which occurs due to charge carrier transitions between localized states.^{23–26} The hopping transport has a strong temperature dependence, as it was observed, e.g., for a network of quasi-metallic 5-AGNRs.²⁷ However, in our devices the temperature dependence of conductance is much weaker than in GNR networks with hopping transport. Increasing the temperature from 4 K to room temperature increases the current by less than one order of magnitude (Fig. 3d and Supplementary Section 5). Therefore, we exclude hopping transport, as well as the thermionic emission over the barrier as the conduction mechanisms in our system. Quantum mechanical tunneling through potential barriers is compatible with the observed dependencies.²⁸ Further evidence that tunneling through 7-AGNR segments governs the transport is the channel length dependence of conduction in our FETs. We observe an exponential drop in I_d with increasing L (Fig. 3e). The exponential trend in I_d differs from the $1/L$ scaling of conductance of an Ohmic conductor. Similarly, for hopping transport through a

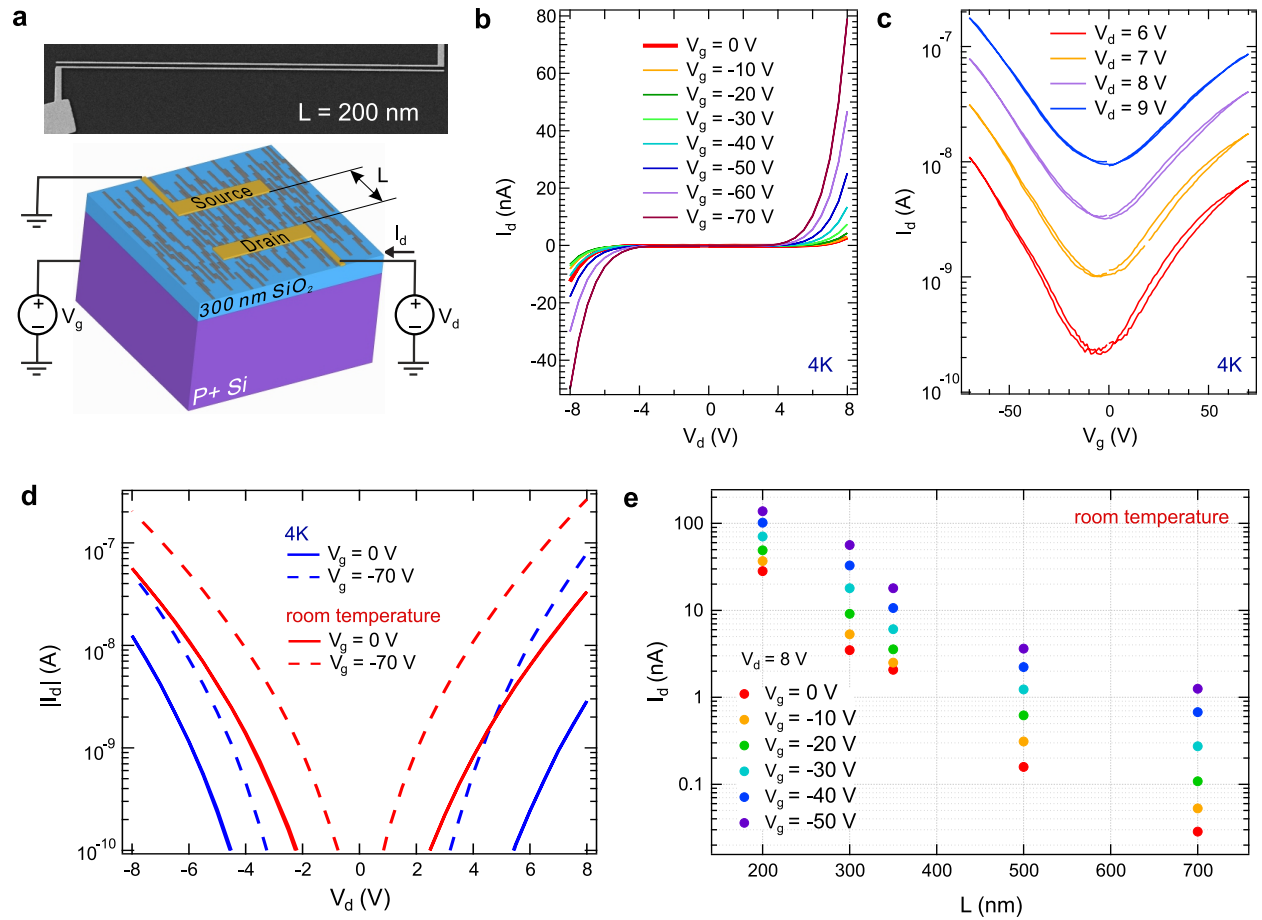


Fig. 3 Charge transport characterization of the transferred GNR heterojunctions. (a) Top: scanning electron microscopy image of the device with $L = 200$ nm and $W = 25$ μm . Bottom: sketch of aligned GNR heterojunctions on SiO_2/Si in a FET geometry with source, drain and gate contacts. (b-d) Transport characteristics of the device with $L = 200$ nm. (b) I_d - V_d curves at different V_g , and (c) I_d versus V_g at different V_d at 4 K. (d) I_d - V_d curves in log scale at 4 K (blue) and room temperature (red) at $V_g = 0$ and -70 V. (e) Channel length dependence of the I_d at $V_d = 8$ V and different V_g at room temperature.

network of metallic GNRs, the measured resistance scales linearly with L .²⁷ If Schottky barriers would dominate the charge transport, all the applied V_d would drop near the contacts. In this situation, I_d - V_d characteristics of devices with different L should be the same, up to multiplication of the current by a constant factor that reflects different numbers of conducting paths in different devices. As a consequence, the slopes of I_d - V_d curves in semilogarithmic plots ($\log(I_d)$ versus V_d) should be independent of the channel length. However, in our data this is not the case, as we will show later. In single semiconducting GNR devices with short contact separation, Schottky barriers led to non-linear I_d - V_d characteristics.²⁹ Our devices have a contact separation $L \geq 200$ nm, and several 7-AGNR barriers are traversed by charge carriers between source and drain. Therefore, these tunneling barriers are expected to dominate device resistance. In the Methods we quantitatively compare the impact of heterojunction barriers and of Schottky barriers on the total device resistance and find that the contribution of the latter is negligible.

Tunneling barrier analysis of transport measurements

We model our system as a set of parallel conducting quasi-metallic 14-AGNRs which are connected in series by 7-AGNR tunneling barriers (Fig. 4a). A voltage V_d across the contacts leads to trapezoidal barrier potential profiles, corresponding to the development of electric field and potential drops across the semiconducting barrier segments. The potential drop per semiconducting segment is $V = V_d/M$ where M is the number of junctions between the contacts. The tunneling of a charge carrier through the barriers is considered to be sequential. A charge carrier entering a 14-AGNR segment following a tunneling event through a 7-AGNR barrier undergoes rapid inelas-

tic scattering through emission of optical phonons. In the related material of carbon nanotubes, charge carriers are scattered by optical phonon emission on length scales estimated to be as short as 10 nm.³⁰ To describe the I_d - V_d characteristics we use the Wentzel-Kramers-Brillouin (WKB) approximation.^{31,32} Equation (4) of Ref. 32 expresses the tunneling current I as a function of the voltage V across a trapezoidal barrier as

$$I(V) = \frac{2e}{h} \int_{-\infty}^{\infty} P(E) [f(E) - f(E + eV)] dE. \quad (1)$$

Here e and h are the electron charge and Planck's constant, respectively. The Fermi distribution function is given by

$$f(E) = \frac{1}{1 + \exp\left(\frac{E - E_F}{kT}\right)}, \quad (2)$$

where E_F depends on V_g and V_d as $E_F(V_g, V_d) = E_F^0(T) + \alpha(T)(V_g + \beta V_d)$. Here E_F^0 , α and β are phenomenological fitting parameters. The parameter α accounts for the modulation of channel potential with V_g , and $\alpha\beta$ accounts for the modulation of channel potential by V_d (see Methods). The quantity $E_F^0(T)$ accounts for the temperature dependence of E_F . $P(E)$ in Eq. (1) is the tunneling probability through the barrier of length d and is given by the following expression:³²

$$P(E) = A \exp\left(-\frac{2}{\hbar} \int_0^d \sqrt{2m[\varphi(x, V) - E]} dx\right). \quad (3)$$

Here $\varphi(x, V) = \Phi_b + (x/d) \cdot (-eV)$ is the barrier height as a function of the coordinate x , Φ_b denotes the barrier height at $x = 0$, and m is the effective mass inside the barrier which we take from ARPES data.²⁰ The prefactor A is proportional to the number of parallel 1D channels across the source-drain contacts and it was not allowed to vary significantly for all devices and it was kept constant for the L -dependent measurements shown below. The barrier height Φ_b is

fixed at a constant value of $\Phi_b = 1.35$ eV for all fits throughout our work (see Methods for determination of Φ_b for GNR heterojunctions on SiO_2). The real GNR heterojunctions system consists of several barriers in sequence where the tunneling current is limited by the longest and most opaque barrier. For simplicity, our model ignores the distribution of d within one device and assumes one effective value of d . Fig. 4b depicts a sketch of the I_d - V_d relations for three barriers with different d indicating that the voltage drop across each barrier becomes closer to each other at high I_d . Thus our model is more accurate in the high I_d - V_d regime. At low I_d and V_d the effects of disorder including the distribution of d and M , trap states, and inhomogeneous surface potential are expected to play a more important role.

Fig. 4c depicts the temperature dependence of the experimental and modeled I_d - V_d characteristics of a $L = 350$ nm device for $T = 4$ K, 100 K, 200 K, and 295 K. The experimental data for $L = 300$ nm, 500 nm and 700 nm devices at different V_g were fitted by restricting the number of tunneling barriers M to be proportional to the channel length L (Fig. 4d-f). In all FETs, the fit yields practically identical values of tunneling barrier length $d \approx 3$ nm. The semilogarithmic plots are shown in the lower panels in Fig. 4d-f. One can see that the slope of the I_d - V_d curves in the semilogarithmic plots decreases with increasing L . This is because of the increase in M and indicates that V_d drops not only at the contacts, but also inside the channel. The semilogarithmic plots reveal a generally worse agreement of the model fit with experiment at small I_d and V_d as discussed in the context of Fig. 4b. Our model accounts for the experimentally observed charge transport behaviour of GNR heterojunctions over a wide range of experimental conditions, including temperature, V_g and length dependence of I_d - V_d characteristics, using a set of only six

fit parameters (A , d , M , $E_f^0(T)$, $\alpha(T)$ and β).

Tunneling current modulation by adsorbates

We performed *in situ* doping of our devices by Li adatoms in a UHV system (Fig. 5a), observing a strong modulation of the transport properties of the GNR heterojunctions. Upon chemical doping by Li, the E_F shifts deeply into the conduction band of quasi-metallic GNRs as schematically shown in Fig. 5b. ARPES spectra of fused GNRs on Au(788) reveal the shift of $VB_1^{14-AGNR}$ relative to E_F by ~ 0.7 eV after deposition of ~ 1 Å of Li, visualizing the partially occupied $CB_1^{14-AGNR}$ (Fig. 5c and Supplementary Section 3). Compared to 14-AGNRs, achieving degenerate electron doping of wide-bandgap 7-AGNRs requires a much larger Li coverage.¹⁹ The I_d - V_d characteristics reveal a dramatic increase in channel current upon Li doping performed in three consecutive steps of ~ 0.1 Å each (Fig. 5d and Supplementary Fig. S6). The I_d - V_d curves of Li doped GNR heterojunctions are accurately reproduced by our tunneling barrier model (Fig. 5d). The surface doping of GNR heterojunctions by Li adatoms shifts E_F and effectively reduces the barrier height to $\Phi_b - E_F$ (Fig. 5e). In the model calculations M and d were held constant. The fit values of E_F for the sample in its pristine state and after Li doses 1–3 were 4 meV, 25 meV, 63 meV and 103 meV relative to $CB_1^{14-AGNR}$, respectively. These values are in good agreement with the shifts inferred by comparison with ARPES (Supplementary Section 6). Our model is also accurately reproducing the I_d - V_d characteristics of the Li doped $L = 500$ nm device (Supplementary Section 6).

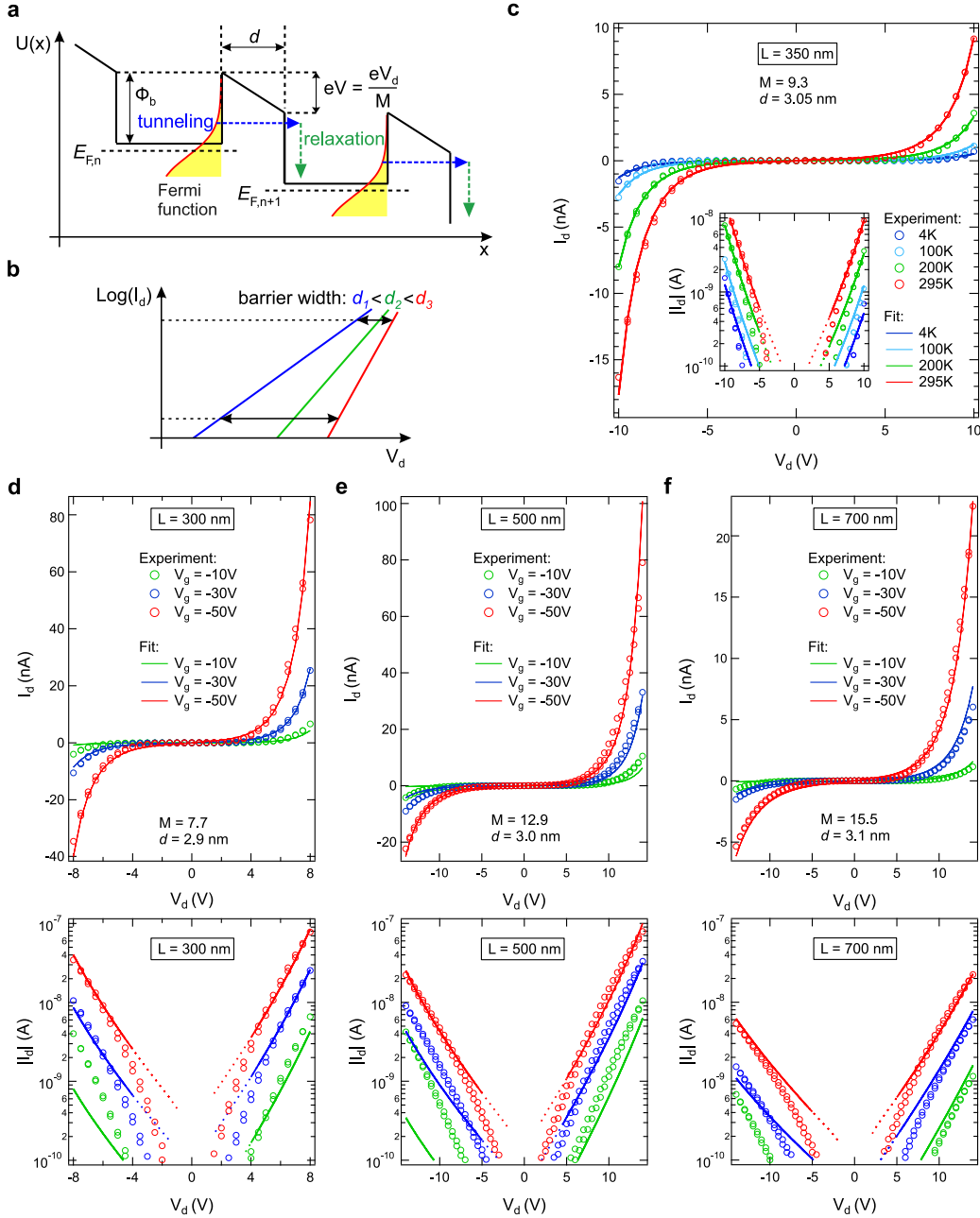


Fig. 4 Comparison of experimental and calculated I_d - V_d curves. (a) The energy diagram along one conducting channel of GNR heterojunctions. The tunneling through a barrier followed by relaxation of the carrier is illustrated. The Fermi level of the n -th barrier is indicated as $E_{F,n}$. The energy drop across one barrier, equal to $eV = eV_d/M$ (where e is the electron charge and M is the number of barriers in the channel), is indicated along with the barrier height Φ_b and the barrier length d . (b) Sketch of $\text{log}(I_d)$ versus V_d characteristics of three different barriers. At high I_d the voltage drops V_d across the barriers assume a narrower distribution (indicated by horizontal arrows). (c) Experimental and calculated I_d - V_d curves of the 350 nm channel device at different temperatures between 4 K and 295 K at $V_g = 0$. The inset shows the I_d - V_d curves in a log scale. (d-f) Experimental and calculated I_d - V_d curves for devices with $L = 300$ nm, 500 nm, and 700 nm at different V_g and at 295 K in a linear (top) and log (bottom) scales.

The channel current through a band conductor scales approximately linearly with charge carrier density. Surface doping of graphene by alkali metal adatoms leads to a modest increase in channel current as a result of the combined effects of increased carrier density and reduced mobility due to charged impurity scattering.³³ In contrast, in an ideal system the tunneling current through a GNR heterojunction is exponentially dependent on the tunneling barrier height. As a consequence, upon alkali metal doping we observe an increase in the current ratios of the doped and pristine samples (I_d/I_{d0}) by a factor 50 for the $L = 200$ nm device operated at $V_d = -6$ V and by a factor 180 for the $L = 500$ nm device operated at $V_d = -14$ V (Fig. 5f). According to our tunneling model, the difference in current modulation for the two devices is mostly related to the voltage drops across one heterojunction (V_d/M) and to the slightly different values of E_F (Supplementary Section 6). We also performed identical adsorption experiments using a graphene FET (Supplementary Section 7). The current in graphene increases only by a factor < 2 after deposition of identical amounts of Li (Fig. 5f). The adsorbate induced current modulation in the GNR heterojunction FETs is highly nonlinear in Li dose. GNR heterojunctions can thus be applied as a new type of sensor that unites the steep slope current scaling of TFETs with an accessible surface for adsorption.

The adsorption of Li modifies the field effect of GNR heterostructures in a non-trivial fashion (Fig. 5g). We observe the loss of bipolar field effect, wherein electron conduction can be modulated by V_g while modulation of hole conduction is strongly suppressed. As illustrated in Fig. 5h, in the pristine system, a “diamond”-like shape emerges in the plot of I_d versus V_g and V_d corresponding to bipolar gate modulation of both electron and hole currents. The “diamond”

is reminiscent of that emerging in Coulomb blockade,³⁴ but is here a direct consequence of the gate modulation of tunneling conduction. Upon Li deposition, I_d no longer exhibits a field effect for $V_g < 0$. For comparison, graphene exhibits a bipolar field effect with a shifted neutrality point after the first Li dose (Fig. S7), in good agreement with previous work in the low-doping regime.³³ At higher Li doses, only electron conduction can be modulated by gate voltage (Fig. S7), in agreement with previous work in the high-doping regime where the mismatch in density of states within bulk and contact graphene regions imparts asymmetry to the field effect.³⁵ The asymmetric field effect in heavily doped GNR heterojunction FETs may thus originate from several mechanisms. In common with graphene, a shift in density of states between bulk and contact regions is expected. Furthermore, Li adsorption can occur on the GNR surfaces, GNR edges, and on the exposed SiO₂ surface, contributing to a more complex environment for charge exchange than graphene. Further work to understand the microscopic mechanisms of field effect in heavily doped GNR heterojunctions is required.

Conclusions

We have synthesized a monolayer film of aligned atomically precise heterojunctions of wide-bandgap and quasi-metallic GNRs on Au(788) and comprehensively characterized them by STM, ARPES and Raman spectroscopy. After the alignment-preserving transfer of the film onto a SiO₂/Si substrate, we have measured charge transport along the GNR heterojunctions in a back-gated FET geometry. The characteristic dependencies of the current on drain and gate voltages, temperature, and channel length indicate that charge transport proceeds by quantum mechanical

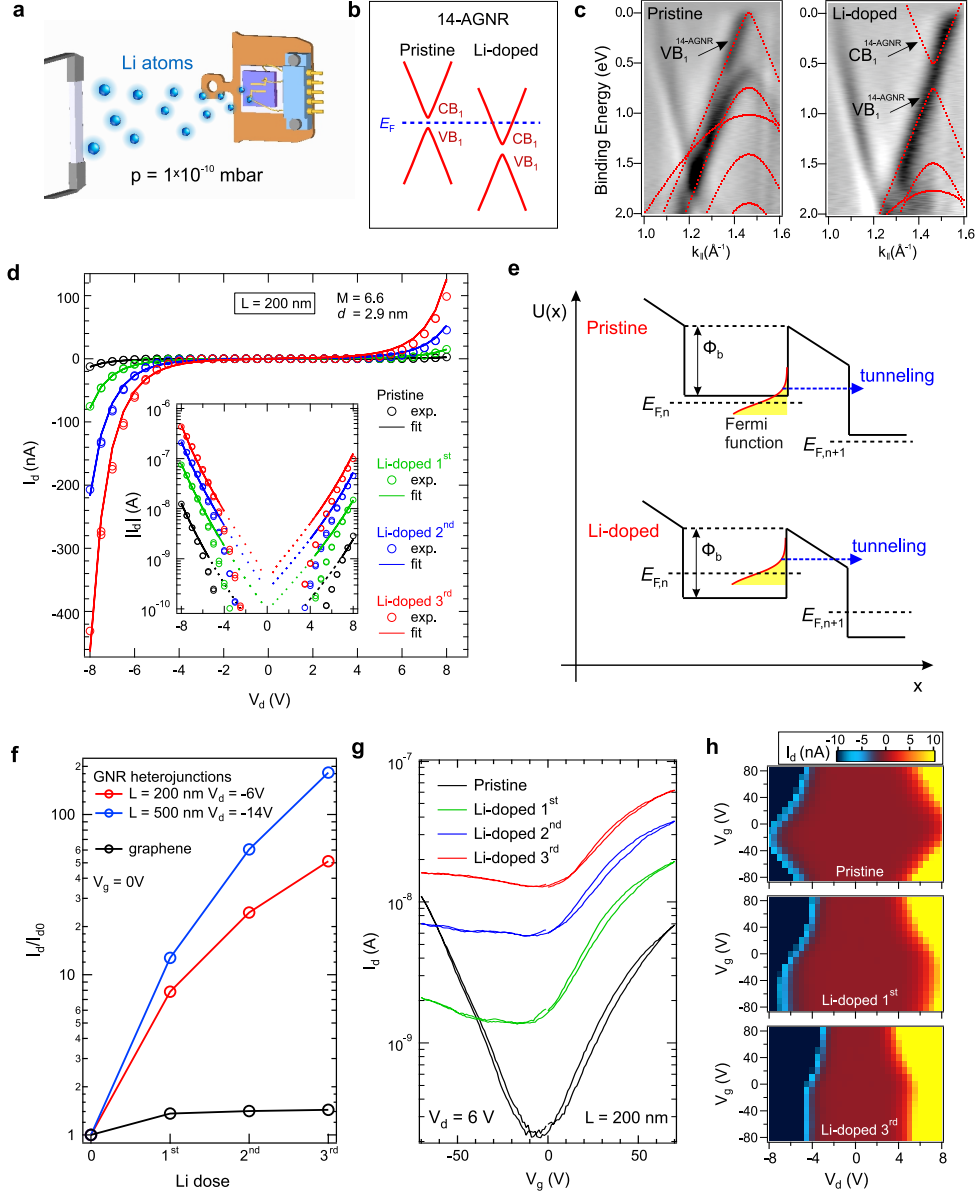


Fig. 5 Band structure and charge transport of Li doped GNR heterojunctions. (a) Sketch of the experimental setup containing a Li source and the GNR heterojunction FET mounted on a UHV compatible sample holder. (b) Sketch of the band structure changes of 14-AGNRs upon Li doping. (c) Second derivatives of ARPES scans by energy of the GNR heterojunctions on Au(788) before (left) and after (right) Li deposition ($\sim 1 \text{ \AA}$) at $k_{\perp} = 0.71 \text{ \AA}^{-1}$ (Supplementary Section 3). (d) I_d - V_d characteristics before (pristine sample) and after deposition of three identical Li doses ($\sim 0.1 \text{ \AA}$ each) in linear and log (inset) scales for the $L = 200 \text{ nm}$ device. Experimental points (exp.) are shown by circles, the fit is indicated by solid lines. (e) Schematic illustration of the potential profile $U(x)$ across a tunneling barrier for pristine and Li doped GNR heterojunctions. (f) The ratio (log scale) of current after Li doping I_d to the current in pristine sample I_{d0} for three Li doses for the $L = 200 \text{ nm}$ device at $V_d = -6 \text{ V}$, for the $L = 500 \text{ nm}$ device at $V_d = -14 \text{ V}$, and for the graphene FET (Supplementary Section 7), all at $V_g = 0 \text{ V}$. (g) I_d - V_g characteristics of the $L = 200 \text{ nm}$ device at $V_d = 6 \text{ V}$ for three Li doses. (h) Color maps of the dependence of I_d on V_g and V_d for pristine and Li doped $L = 200 \text{ nm}$ device. All transport measurements were performed at 4 K.

tunneling through the wide-bandgap 7-AGNR segments in the GNR heterojunctions. The experimental transport data are in agreement with computations (WKB approximation) of the tunneling current through multiple tilted barriers. Our model is able to describe all observed experimental current-voltage characteristics in the high bias regime using a minimal set of fit parameters including the effective barrier height, the junction length, and the number of junctions. We have demonstrated that the adsorption of atoms on the GNR heterojunction surface strongly modulates the tunneling conductance by charge transfer doping. We employed the steep slope response of GNR heterojunction based tunnel FETs with their accessible surface area to realize a nanoelectronic sensor with a giant sensitivity to adsorbates. Our results are important not only for applications of bottom-up synthesised carbon nanomaterials but for the wider nanoscience community that applies low-dimensional materials in new device concepts.

Methods

Growth of GNR heterojunctions The synthesis of aligned GNR heterojunctions for our tunneling devices consists of the following steps: 1) deposition of approximately one monolayer coverage of 10,10-dibromo-9,9 bianthracene (DBBA) molecules on a clean Au(788) surface (prepared by standard Ar⁺ sputtering and annealing cycles) in UHV; 2) dehalogenation of the precursor molecules and assembly of the aligned polymer chains by annealing at $\sim 200^\circ\text{C}$ for 10 min.; 3) cyclodehydrogenation and lateral fusion at $\sim 410^\circ\text{C}$ for 180 min. The first two steps are identical to the synthesis of densely aligned 7-AGNRs on Au(788) ^{18,20,22} while the third step is performed at higher temperature and longer annealing time. The annealing temperature and time

were optimized to get a maximum amount of 14-AGNRs using *in situ* studies with UHV Raman spectroscopy (Supplementary Section 4).

STM measurements STM imaging was done at room temperature and in UHV (base pressure was 4×10^{-11} mbar) in the Athene STM chamber in Cologne. The STM images were processed (background subtraction and contrast adjustment) using the WSxM software.³⁶

ARPES experiments During ARPES experiments the base pressure was below 2×10^{-10} mbar. In all experiments the aligned GNR heterojunctions were oriented along the slit of analyzer and linearly horizontally polarized light was used. The ARPES measurements shown in Fig. 2b and Figs. S2a-e have been performed at Hiroshima Synchrotron Radiation Center (beamline BL-9A/B) using a horizontal analyzer slit and the tilt angle of manipulator to tune k_{\perp} at 10 K with the photon energy of 25 eV. The GNR synthesis and fusion were performed *in situ*. ARPES experiments on Li doping and the ARPES data shown in Fig. S2f-i have been performed at HZB BESSY II (UE112-PGM2 beamline, 1²-ARPES end-station) using a vertical analyzer slit and the polar angle of manipulator to tune k_{\perp} at room temperature with the photon energy of 45 eV. The sample was synthesized at the University of Cologne and preliminary checked *in situ* by UHV Raman spectroscopy. Then the sample was transferred to the ARPES end-station in the suitcase filled by Ar. Li doping was performed *in situ* using a SAES getter. The amount of deposited Li, estimated by a quartz crystal microbalance sensor, was about 1 Å.

Energy band structure calculations and ARPES intensity simulations Density-functional-theory (DFT) calculations of the band structure of 7-AGNRs and 14-AGNRs were carried out using the

FPLO-14.00-48 code (improved version of the original FPLO code by Koepnik and Eschrig)³⁷ utilizing the generalized gradient approximation (GGA) to the exchange-correlation potential. The GNRs were assumed freestanding and hydrogen-terminated. A k -point grid of $12 \times 1 \times 1$ was used to sample the Brillouin zone. Atomic positions were relaxed until the forces on each atom were less than 10^{-2} eV/Å. The calculated electronic bands of 7-AGNRs and 14-AGNRs that are shown in Fig. 2b were shifted in energy to match the experimental VB_1 . The photoemission intensity that is shown in Fig. S2 was calculated using the dipole approximation for the matrix element with a plane wave as a final state.^{20,38}

Raman spectroscopy measurements All Raman measurements presented in this work were performed in the back-scattering geometry using a Renishaw inVia setup with a 633 nm laser at room temperature. UHV Raman studies shown in Fig. 2 were performed in the same setup where the GNR heterojunctions were synthesized.¹⁹ In the UHV studies, the laser was polarized along the GNR alignment direction (z), and the collected Raman signal was a sum over the GNR plane (zz and zy). UHV Raman data were acquired using a $50\times$ long-working distance objective with a numerical aperture of 0.4, and the laser power of 7 mW. This laser power does not affect the sample quality due to the UHV conditions. Polarized Raman measurements of the GNR heterojunctions transferred onto the SiO_2/Si substrate, shown in Fig. S4d, were performed in ambient conditions using a $50\times$ objective and 0.4 mW laser power. The low wavenumber data, shown in Fig. S4c, were acquired with the laser polarized along the alignment direction of GNR heterojunctions using a notch filter and 0.8 mW laser power.

Calculation of Raman spectra Theoretical modeling of the Raman spectra has been performed in the framework of DFT. All computations were carried out within the AIMPRO DFT package.^{39,40} Perdew-Burke-Ernzerhof generalized gradient approximation (PBE-GGA)⁴¹ has been used as exchange-correlation functional. The action of core electrons was modeled using Hartwigsen-Goedecker-Hutter pseudopotentials⁴² and the electron wave functions have been expanded into a basis set of Gaussian orbitals. The carbon atom basis consisted of 38 *s*-, *p*- and *d*-type functions, whereas for hydrogen a total of 12 *s*- and *p*-type functions were used. A *k*-point grid with the resolution of $2\pi \times 0.01 \text{ \AA}^{-1}$ along the periodic direction of the GNR has been employed for the self-consistent field cycle. After geometry optimization, phonon eigenvalues and eigenvectors from the Brillouin zone center have been calculated with the use of the finite-displacement method. The Raman tensor has been calculated by considering finite atomic displacements along the phonon eigenvectors and by calculating the frequency-dependent dielectric tensor for each eigenmode. For the dielectric tensor calculation, a fine *k*-point grid with a resolution of $2\pi \times 0.0006 \text{ \AA}^{-1}$ along the GNR axis has been used. A scissor shift for the bandgap has been applied in order to bring the calculated gap values in closer agreement with experiment (2.1 eV for 7-AGNR and ~ 0.25 eV for 14-AGNR). The Raman intensity for the *j*-th mode at excitation energy E_{exc} was obtained as $I \propto \frac{n_j+1}{\omega_j} |\mathbf{e}_i \cdot \mathbf{R}_j(E_{\text{exc}}) \cdot \mathbf{e}_s^T|^2$, where ω_j is the phonon frequency, $n_j = (e^{\hbar\omega_j/k_B T} - 1)^{-1}$ is the Bose-Einstein distribution function at $T = 300$ K, \mathbf{e}_i and \mathbf{e}_s are electric polarization vectors of the incident and scattered optical fields, respectively, and $\mathbf{R}_j(E_{\text{exc}})$ is the Raman tensor of phonon mode *j* at excitation energy E_{exc} . In the experimental scattering geometry, the incident light is polarized along the periodic GNR axis *z*, and the scattered light is collected in the

GNR zy plane. After averaging over the scattered polarizations, the Raman intensities are given as $I \propto 0.5 \frac{n_j+1}{\omega_j} (|R_{zz,j}(E_{exc})|^2 + |R_{zy,j}(E_{exc})|^2)$. For the plots of Raman spectra, Lorentzian broadening of the peaks has been applied.

Device fabrication The devices were prepared on highly doped single-side polished Si substrates with 300 nm thick thermally grown SiO_2 . First, $150 \times 150 \mu\text{m}^2$ -sized contact pads were patterned using optical lithography. For the contact pads we used 10 nm of titanium for adhesion followed by 50 nm of gold. Subsequently the aligned GNR heterojunction film was transferred with known orientation onto the substrate.²² The GNR alignment was checked by polarized Raman measurements (Supplementary Section 4). Electron beam lithography was used to define the source and drain electrodes. For this purpose the samples were coated with a double layer of PMMA. The bottom layer (molecular weight 250 kg/mol) is more sensitive than the top layer (molecular weight 950 kg/mol), resulting in an undercut that facilitates lift-off processing. The PMMA-coated substrates were exposed in an electron beam writer, developed, and a 10 nm layer of titanium and 30 nm layer of gold were deposited by thermal evaporation. Subsequently the metal was removed from the unexposed regions of the sample using a lift-off process.

UHV transport characterization Prior to the UHV transport characterization, the SiO_2/Si wafers with GNR heterojunction devices were glued (silver epoxy) onto sapphire plates which were mounted onto omicron-type sample holders. The sample holders were equipped with five spring-contact pins mounted at one end (see Fig. 5a). The source and drain contact pads on the sample were each connected by $25 \mu\text{m}$ Au wire with one pin of the spring contact. Similarly, the back gate

contact was attached to one pin. Upon insertion into the UHV cryostat sample receptacle, the five pins make contact with BNC type feedthroughs that connect the device inside the UHV chamber to the electronics outside. For each device, we only used three pins (source, drain and gate). For the application of V_g and the measurement of the gate leakage current, a Keithley 2400 source measure unit (SMU) was employed. Another SMU of the same type was used for the application of V_d and the measurement of I_d . Field-effect mobility was determined as: $\mu_{\text{DTM}} = g_m(L/W)(1/C_g V_d)$, where C_g is the capacitance per unit area of the SiO_2 back-gate dielectric and $g_m = \partial I_d / \partial V_g$ is the transconductance.

Schottky and tunneling barrier heights In our FETs, charge carriers are injected from the metal source contact to either quasi-metallic (14-AGNRs, 21-AGNRs, ...) or semiconducting 7-AGNR segments and then transported through a sequence of 7-AGNRs tunneling barriers. Below we compare the Schottky barrier heights of the 14-AGNR/metal and the 7-AGNR/metal contacts with the tunneling barrier height Φ_b . The estimation of the Schottky barriers for carrier injection from the contacts to GNRs and the tunneling barrier Φ_b requires the information of the transport bandgap and the valence and conduction band offsets (VB_1 and CB_1 , respectively). The transport bandgap strongly depends on the substrate via the screening of the Coulomb interaction^{43,44}. As a consequence the bandgap can range from $\sim 2.3\text{--}2.5$ eV for 7-AGNRs on Au(111) substrate to $\sim 3.7\text{--}3.9$ eV for isolated 7-AGNRs.^{14,43-46} The bandgap of 14-AGNRs on Au is ~ 0.2 eV and for an isolated 14-AGNR it is around 0.7 eV.¹⁴ For 7-AGNRs on SiO_2 theory predicts that the bandgap is ~ 3.3 eV, that is about 85% smaller than for the isolated 7-AGNR.⁴⁴ If we scale down the bandgap for isolated 14-AGNRs by 85% we obtain 0.6 eV, which is valid for 14-AGNRs on SiO_2 .

For estimation of the tunneling barrier Φ_b on SiO_2 , we assume electron-hole symmetry with the chemical potential of 7-AGNRs and 14-AGNRs lying symmetrically in the gap. This estimation yields $\Phi_b = 1.35$ eV as a tunneling barrier for both, electrons and holes and ignores the effects of charged impurities in the SiO_2 that may affect the GNR bandgap and the position of E_F .⁴⁷

We assume that the metal contacts in our FETs provide the same screening as the Au substrate used for GNR synthesis, and result in the same bandgaps and energy offsets for the VB_1 and CB_1 . The VB_1 and CB_1 in turn provide the Schottky barriers for hole and electron injection, respectively. The GNR bandgaps at the contact region are just $E_g^{7\text{-AGNR}} = 2.4$ eV and $E_g^{14\text{-AGNR}} = 0.2$ eV for 7-AGNRs and 14-AGNRs, respectively, as derived from scanning tunneling spectroscopy measurements.^{12,14,45} It is thus clear that the Schottky barrier for the 14-AGNR/metal interface is much smaller compared to the Φ_b , and therefore has negligible effect in our devices. For 7-AGNRs/metal interface from the ARPES spectra we obtain $\text{VB}_1^{7\text{-AGNR}} = 0.8$ eV,²⁰ and since $\text{CB}_1^{7\text{-AGNR}} = E_g^{7\text{-AGNR}} - \text{VB}_1^{7\text{-AGNR}}$, we have $\text{CB}_1^{7\text{-AGNR}} = 1.6$ eV. Therefore, the Schottky barriers for 7-AGNR/metal for electron and hole injection are 1.6 eV and 0.8 eV, respectively. The Schottky barrier for the 7-AGNR to metal contacts is comparable to Φ_b . Considering that we have many more heterojunctions than Schottky barriers between source and drain, GNR heterojunctions dominate device resistance.

Model for tunneling transport To calculate the tunneling probability $P(E)$ through a trapezoidal barrier, we used the following expression: ³²

$$\begin{aligned} P(E) &= A \exp \left(-\frac{2}{\hbar} \int_0^d \sqrt{2m[\varphi(x, V) - E]} dx \right) \\ &= A \exp \left(-\frac{4d\sqrt{2m}}{3\hbar eV} [(\Phi_b - E)^{3/2} - (\Phi_b - E - eV)^{3/2}] \right). \end{aligned} \quad (4)$$

This equation is valid only for the case when the tunneling occurs between the edges of the barrier, i.e., the tunneling length is equal to the geometrical length of the barrier d . This is the case if $\Phi_b - E > 0$ and $\Phi_b - E - eV > 0$. Depending on the sign of V_d , the barrier can either decrease or increase by the amount $|eV|$ along the tunneling path. Since the situation is symmetrical with respect to the direction of the applied voltage, we will consider in the following the case of $V \geq 0$. In the case $\Phi_b - E > 0$ and $\Phi_b - E - eV < 0$, the carrier has to tunnel under the triangular barrier and the transmission coefficient is described by the Fowler-Nordheim theory ⁴⁸. In Eq. (4), d indicates the barrier length, m is the charge carrier effective mass inside the barrier, $\varphi(x, V) = \Phi_b + (x/d) \cdot (-eV)$ is barrier height at coordinate x and V is the applied voltage, Φ_b denotes the barrier height at $x = 0$. In the case of a triangular barrier, the integration over x in the exponent of Eq. (3) should be performed from zero till the value x_c determined by the condition $\varphi(x_c, V) - E = 0$. The expression for $P(E)$ then reads,

$$P(E) = A \exp \left(-\frac{4d\sqrt{2m}}{3\hbar eV} (\Phi_b - E)^{3/2} \right), \quad (5)$$

in agreement with the exponent in Eq. (4) of Ref. 28. The integral over E in Eq. (1) is to be calculated in the range $E \geq 0$, $E \geq -eV$. This integration was performed numerically. The position of the Fermi level E_F in Eq. (1) is determined by the carrier concentration in the channel

which in turn is controlled by V_g . The carrier concentration n in the channel of the heterojunction FET is given by $n = n_0 + V_g C_g / e$. Approximating the density of states by a constant ρ we have $n - n_0 = \rho(E_F - E_F^0)$ where $n - n_0$ is the change in the carrier concentration induced by the gate voltage and $E_F - E_F^0$ is the Fermi level shift induced by the gate voltage. Rearranging the above equation yields $E_F = E_F^0 + (n - n_0) / \rho$. Substituting $n = n_0 + V_g C_g / e$ we get $E_F = E_F^0 + C_g V_g / (e\rho)$. We set $\alpha = C_g / (e\rho)$ and take into account that the source-drain voltage also affects the gate potential at a given position along the channel. For instance, a barrier close to the source contact experiences a different potential than a barrier close to the drain contact. Thus the gate voltage dependence is modeled in our fit as $E_F(V_g, V_d) = E_F^0(T) + \alpha(T)(V_g + \beta V_d)$. This relation assumes that the E_F is a linear function of carrier concentration which is always true for a sufficiently small range of E_F , e.g., for a small gate voltage range. In all our fits of I_d - V_d curves, the variation of E_F^0 was within 100 meV relative to band edge, i.e. small as compared to Φ_b . The product $\alpha\beta$ accounts for the asymmetry between the source and drain contacts, with the former taken as the reference potential against which both gate potential V_g and drain potential V_d are applied.

Data availability

The datasets generated during and/or analysed during the current study are available from the corresponding author on reasonable request.

Supplementary information

Supplementary Sections 1-7, Figures S1-S7 and Supplementary References.

Author contributions

BS and AG planned the research and organized the experimental work. BS fabricated the GNR heterojunction samples and characterized them by UHV Raman spectroscopy and UHV transport. PB and TM performed STM measurements. BS and AG performed ARPES measurements of *in situ* fused GNRs. BS and AVF performed ARPES measurements of Li doped GNRs. AN, SDB and FG performed the calculations of the tunneling current. MH, YF, BS, TS, and AG built a UHV compatible electronic transport measurement setup and participated in the transport measurements. AC contributed to the UHV Raman experiments on the GNR fusion. BS analyzed the Raman and ARPES data. BS, AN, SB, KL, TS and AG interpreted the transport data. SA and KL fabricated the electrode structures for the FETs. DR performed the calculations of the Raman spectra. DU performed the DFT calculations of the GNR band structure and simulations of the ARPES intensity. AVF, TO, KM, MA and KS operated the ARPES beamlines. FRF synthesized precursor molecules. All co-authors contributed to the discussion of the data. BS, TS, and AG wrote the manuscript with input from all co-authors.

Competing Interests The authors declare that they have no competing interests.

Acknowledgements BS, YF and AG acknowledge the ERC-grant no. 648589 'SUPER-2D'. AG and KL acknowledge DFG projects GR 3708/4-1 and LI 2633/5-1. TS acknowledges support from "Quantum Matter and Materials" for a long-time stay in Cologne. AN acknowledges support from the Russian Foundation for Basic Research (project 20-52-00016 Bel-a). SKA acknowledges Bonn Cologne Graduate School (BCGS) of Physics and Astronomy and DAAD for financial support. KL and SKA acknowledge a grant

from the Volkswagen Foundation. PB acknowledges financial support from the Alexander von Humboldt foundation. DU acknowledges Saint Petersburg State University (Grant No. ID 51126254). We acknowledge the Hiroshima synchrotron radiation facility for providing access to its facilities (proposal 17BG018). We also acknowledge HZB BESSY II for the provision of synchrotron radiation. AC acknowledges support by the Alexander-von-Humboldt-Stiftung. Research is supported by the U.S. Department of Energy, Office of Science, Basic Energy Sciences, under Award DE-SC0010409 (design, synthesis, and characterization of molecular precursors).

Correspondence Correspondence and requests for materials should be addressed to BS, TS, and AG (email: senkovskiy@ph2.uni-koeln.de, thomas.szkopek@mcgill.ca, and grueneis@ph2.uni-koeln.de).

References

1. Alferov, Z. I. Nobel Lecture: The double heterostructure concept and its applications in physics, electronics, and technology. Rev. Mod. Phys. **73**, 767–782 (2001). URL <https://link.aps.org/doi/10.1103/RevModPhys.73.767>.
2. Kroemer, H. Nobel Lecture: Quasielectric fields and band offsets: teaching electrons new tricks. Rev. Mod. Phys. **73**, 783–793 (2001). URL <https://link.aps.org/doi/10.1103/RevModPhys.73.783>.
3. Esaki, L. & Tsu, R. Superlattice and negative differential conductivity in semiconductors. IBM J. Res. Dev. **14**, 61–65 (1970). URL <https://doi.org/10.1147/rd.141.0061>.

4. Kazarinov, R. E. & Suris, R. A. Possibility of amplification of electromagnetic waves in a semiconductor superlattice. Fiz. Tekh. Polupr. **5**, 798 – 800 (1971). (Sov. Phys.: Semicond. **5**, 707, 1971).
5. Faist, J. et al. Quantum Cascade Laser. Science **264**, 553–556 (1994). URL <http://science.sciencemag.org/content/264/5158/553.abstract>.
6. Geim, A. K. & Grigorieva, I. V. Van der Waals heterostructures. Nature **499**, 419 – 425 (2013). URL <https://doi.org/10.1038/nature12385>.
7. Novoselov, K. S., Mishchenko, A., Carvalho, A. & Castro Neto, A. H. 2D materials and van der Waals heterostructures. Science **353**, aac9439 (2016). URL <https://science.sciencemag.org/content/353/6298/aac9439>.
8. Huang, H. et al. Spatially Resolved Electronic Structures of Atomically Precise Armchair Graphene Nanoribbons. Sci. Rep. **2**, 983 (2012). URL <https://doi.org/10.1038/srep00983>.
9. Cai, J. et al. Graphene nanoribbon heterojunctions. Nat. Nanotechnol. **9**, 896–900 (2014). URL <https://doi.org/10.1038/nnano.2014.184>.
10. Chen, Y.-C. et al. Molecular Bandgap Engineering of Bottom-up Synthesized Graphene Nanoribbon Heterojunctions. Nat. Nanotechnol. **10**, 156–160 (2015). URL <https://doi.org/10.1038/nnano.2014.307>.

11. Nguyen, G. D. et al. Atomically precise graphene nanoribbon heterojunctions from a single molecular precursor. Nat. Nanotechnol. **12**, 1077–1082 (2017). URL <http://dx.doi.org/10.1038/nnano.2017.155>.
12. Ma, C. et al. Seamless Staircase Electrical Contact to Semiconducting Graphene Nanoribbons. Nano Lett. **17**, 6241–6247 (2017). URL <https://doi.org/10.1021/acs.nanolett.7b02938>.
13. Jacobse, P. H. et al. Electronic components embedded in a single graphene nanoribbon. Nat. Commun. **8**, 119 (2017). URL <https://doi.org/10.1038/s41467-017-00195-2>.
14. Wang, S. et al. Quantum Dots in Graphene Nanoribbons. Nano Lett. **17**, 4277–4283 (2017). URL <https://doi.org/10.1021/acs.nanolett.7b01244>.
15. Vadlamani, S. K. et al. Tunnel-FET Switching Is Governed by Non-Lorentzian Spectral Line Shape. Proc. IEEE 1–10 (2019). URL <https://doi.org/10.1109/jproc.2019.2904011>.
16. Zhang, Q., Fang, T., Xing, H., Seabaugh, A. & Jena, D. Graphene nanoribbon tunnel transistors. IEEE Electron Device Lett. **29**, 1344–1346 (2008). URL <https://doi.org/10.1109/LED.2008.2005650>.
17. Ionescu, A. M. & Riel, H. Tunnel field-effect transistors as energy-efficient electronic switches. Nature **479**, 329–337 (2011). URL <https://doi.org/10.1038/nature10679>.

18. Linden, S. et al. Electronic Structure of Spatially Aligned Graphene Nanoribbons on Au(788). Phys. Rev. Lett. **108**, 216801 (2012). URL <https://doi.org/10.1103/PhysRevLett.108.216801>.
19. Senkovskiy, B. V. et al. Semiconductor-to-Metal Transition and Quasiparticle Renormalization in Doped Graphene Nanoribbons. Adv. Electron. Mater. **3**, 1600490 (2017). URL <https://doi.org/10.1002/aelm.201600490>.
20. Senkovskiy, B. V. et al. Finding the Hidden Valence Band of N=7 Armchair Graphene Nanoribbons with Angle-Resolved Photoemission Spectroscopy. 2D Mater. **5**, 035007 (2018). URL <https://doi.org/10.1088/2053-1583/aabb70>.
21. Merino-Díez, N. et al. Width-Dependent Band Gap in Armchair Graphene Nanoribbons Reveals Fermi Level Pinning on Au(111). ACS Nano **11**, 11661–11668 (2017). URL <https://doi.org/10.1021/acsnano.7b06765>.
22. Senkovskiy, B. V. et al. Making Graphene Nanoribbons Photoluminescent. Nano Lett. **17**, 4029–4037 (2017). URL <https://doi.org/10.1021/acs.nanolett.7b00147>.
23. Pollak, M. A percolation treatment of dc hopping conduction. J. Non-Cryst. Solids **11**, 1–24 (1972). URL <http://www.sciencedirect.com/science/article/pii/0022309372903043>.
24. Mott, N. F. The effect of electron interaction on variable-range hopping. Phil. Mag. **34**, 643–645 (1976). URL <https://doi.org/10.1080/14786437608223801>.

25. Zabrodskii, A. G. The Coulomb gap: The view of an experimenter. Philos. Mag. B **81**, 1131–1151 (2001). URL <https://doi.org/10.1080/13642810108205796>.
26. Nenashev, A. V., Oelerich, J. O. & Baranovskii, S. D. Theoretical tools for the description of charge transport in disordered organic semiconductors. J. Phys.: Condens. Matter **27**, 093201 (2015). URL <http://dx.doi.org/10.1088/0953-8984/27/9/093201>.
27. Richter, N. et al. Charge transport mechanism in networks of arm-chair graphene nanoribbons. Sci. Rep. **10**, 1988 (2020). URL <https://doi.org/10.1038/s41598-020-58660-w>.
28. Tuomisto, N., Zugarramurdi, A. & Puska, M. J. Modeling of electron tunneling through a tilted potential barrier. J. Appl. Phys. **121**, 134304 (2017). <https://doi.org/10.1063/1.4979533>.
29. Llinas, J. P. et al. Short-channel field-effect transistors with 9-atom and 13-atom wide graphene nanoribbons. Nat. Commun. **8**, 633 (2017). URL <https://doi.org/10.1038/s41467-017-00734-x>.
30. Yao, Z., Kane, C. L. & Dekker, C. High-Field Electrical Transport in Single-Wall Carbon Nanotubes. Phys. Rev. Lett. **84**, 2941–2944 (2000). URL <https://link.aps.org/doi/10.1103/PhysRevLett.84.2941>.
31. Harrison, W. A. Tunneling from an Independent-Particle Point of View. Phys. Rev. **123**, 85–89 (1961). URL <https://link.aps.org/doi/10.1103/PhysRev.123.85>.

32. Brinkman, W. F., Dynes, R. C. & Rowell, J. M. Tunneling Conductance of Asymmetrical Barriers. J. Appl. Phys. **41**, 1915–1921 (1970). URL <https://doi.org/10.1063/1.1659141>.
33. Chen, J.-H. et al. Charged-impurity scattering in graphene. Nat. Phys. **4**, 377–381 (2008). URL <https://doi.org/10.1038/nphys935>.
34. El Abbassi, M. et al. Controlled Quantum Dot Formation in Atomically Engineered Graphene Nanoribbon Field-Effect Transistors. ACS Nano **14**, 5754–5762 (2020). URL <https://doi.org/10.1021/acsnano.0c00604>.
35. Farmer, D. B. et al. Chemical Doping and Electron-Hole Conduction Asymmetry in Graphene Devices. Nano Lett. **9**, 388–392 (2009). URL <https://doi.org/10.1021/nl803214a>.
36. Horcas, I. et al. Wsxn: A software for scanning probe microscopy and a tool for nanotechnology. Rev. Sci. Instrum. **78**, 013705 (2007). URL <https://doi.org/10.1063/1.2432410>.
37. Koepernik, K. & Eschrig, H. Full-potential Nonorthogonal Local-orbital Minimum-basis Band-structure Scheme. Phys. Rev. B **59**, 1743–1757 (1999). URL <https://doi.org/10.1103/PhysRevB.59.1743>.
38. Senkovskiy, B. V. et al. Spectroscopic Characterization of $N = 9$ Armchair Graphene Nanoribbons. Phys. Status Solidi RRL **11**, 1700157 (2017). URL <https://doi.org/10.1002/pssr.201700157>.

39. Rayson, M. J. & Briddon, P. R. Highly efficient method for Kohn-Sham density functional calculations of 500 – 10 000 atom systems. Phys. Rev. B **80**, 205104 (2009). URL <https://link.aps.org/doi/10.1103/PhysRevB.80.205104>.
40. Briddon, P. R. & Rayson, M. J. Accurate Kohn-Sham DFT with the speed of tight binding: Current techniques and future directions in materials modelling. Phys. Status Solidi B **248**, 1309–1318 (2011). URL <https://doi.org/10.1002/pssb.201046147>.
41. Perdew, J. P., Burke, K. & Ernzerhof, M. Generalized Gradient Approximation Made Simple. Phys. Rev. Lett. **77**, 3865–3868 (1996). URL <https://link.aps.org/doi/10.1103/PhysRevLett.77.3865>.
42. Hartwigsen, C., Goedecker, S. & Hutter, J. Relativistic separable dual-space Gaussian pseudopotentials from H to Rn. Phys. Rev. B **58**, 3641–3662 (1998). URL <https://link.aps.org/doi/10.1103/PhysRevB.58.3641>.
43. Yang, L., Park, C.-H., Son, Y.-W., Cohen, M. L. & Louie, S. G. Quasiparticle Energies and Band Gaps in Graphene Nanoribbons. Phys. Rev. Lett. **99**, 186801 (2007). URL <https://doi.org/10.1103/PhysRevLett.99.186801>.
44. Kharche, N. & Meunier, V. Width and Crystal Orientation Dependent Band Gap Renormalization in Substrate-Supported Graphene Nanoribbons. J. Phys. Chem. Lett. **7**, 1526–1533 (2016). URL <https://doi.org/10.1021/acs.jpcllett.6b00422>.
45. Ruffieux, P. et al. Electronic Structure of Atomically Precise Graphene Nanoribbons. ACS Nano **6**, 6930–6935 (2012). URL <https://doi.org/10.1021/nn3021376>.

46. Denk, R. et al. Exciton-dominated Optical Response of Ultra-narrow Graphene Nanoribbons. Nat. Commun. **5**, 4253 (2014). URL <https://doi.org/10.1038/ncomms5253>.
47. Samaddar, S., Yudhistira, I., Adam, S., Courtois, H. & Winkelmann, C. B. Charge Puddles in Graphene near the Dirac Point. Phys. Rev. Lett. **116**, 126804 (2016). URL <https://link.aps.org/doi/10.1103/PhysRevLett.116.126804>.
48. Fowler, R. H. & Nordheim, L. Electron emission in intense electric fields. Proc. Roy. Soc. Lond. **A119**, 173–181 (1928). URL <https://doi.org/10.1098/rspa.1928.0091>.

Figures

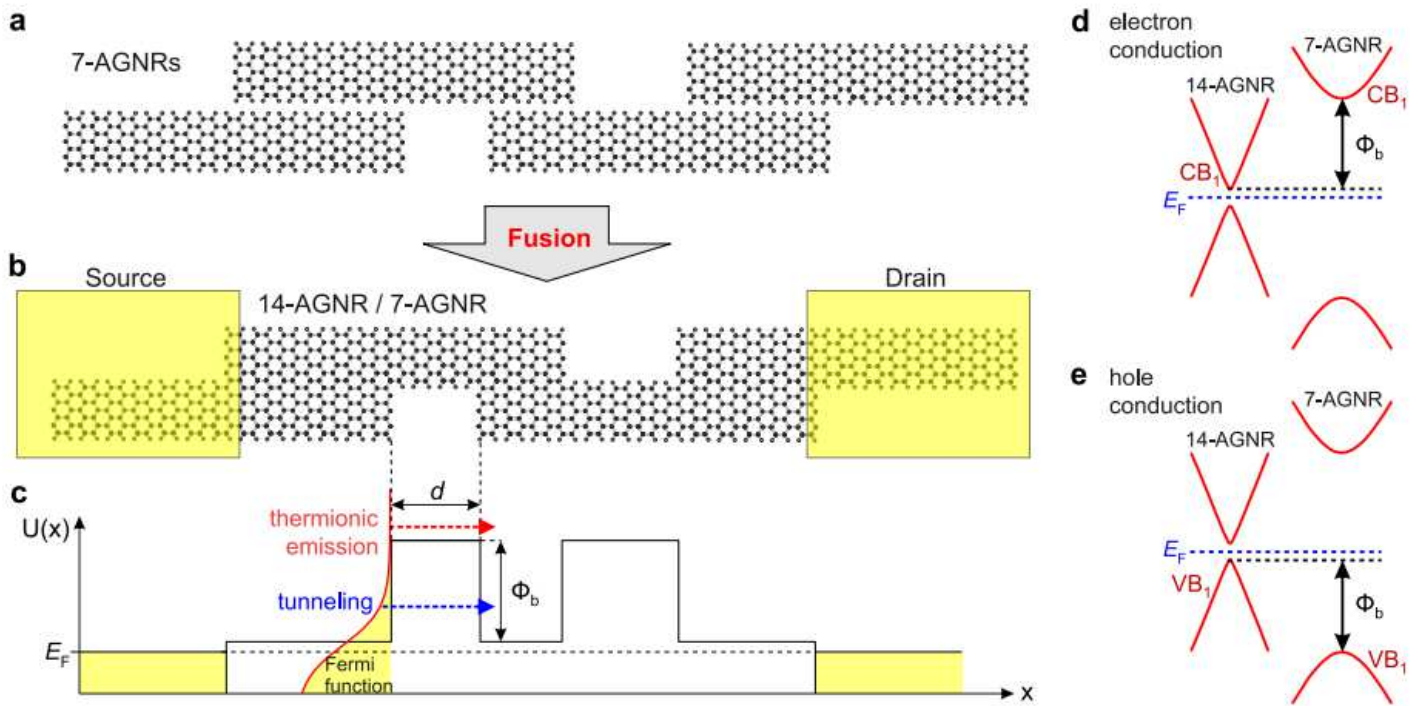


Figure 1

Fabrication and electronic structure of GNR heterojunctions. (a, b) Schematic illustration of the lateral fusion that forms 14-AGNR segments from two adjacent 7-AGNRs. When the source-drain contacts are fabricated, the remaining 7-AGNR segments act as tunneling barriers. (c) Potential $U(x)$ as a function of coordinate x between source and drain contacts of multiple 7-/14-AGNR heterojunctions. The barrier height Φ_b and the barrier length d are indicated. Thermionic emission and tunneling mechanisms are schematically shown. (d, e) Sketch of the electronic energy band dispersions of 7-AGNR and 14-AGNR. The conduction and valence band edges are CB_1 and VB_1 , respectively, and determine the value of Φ_b .

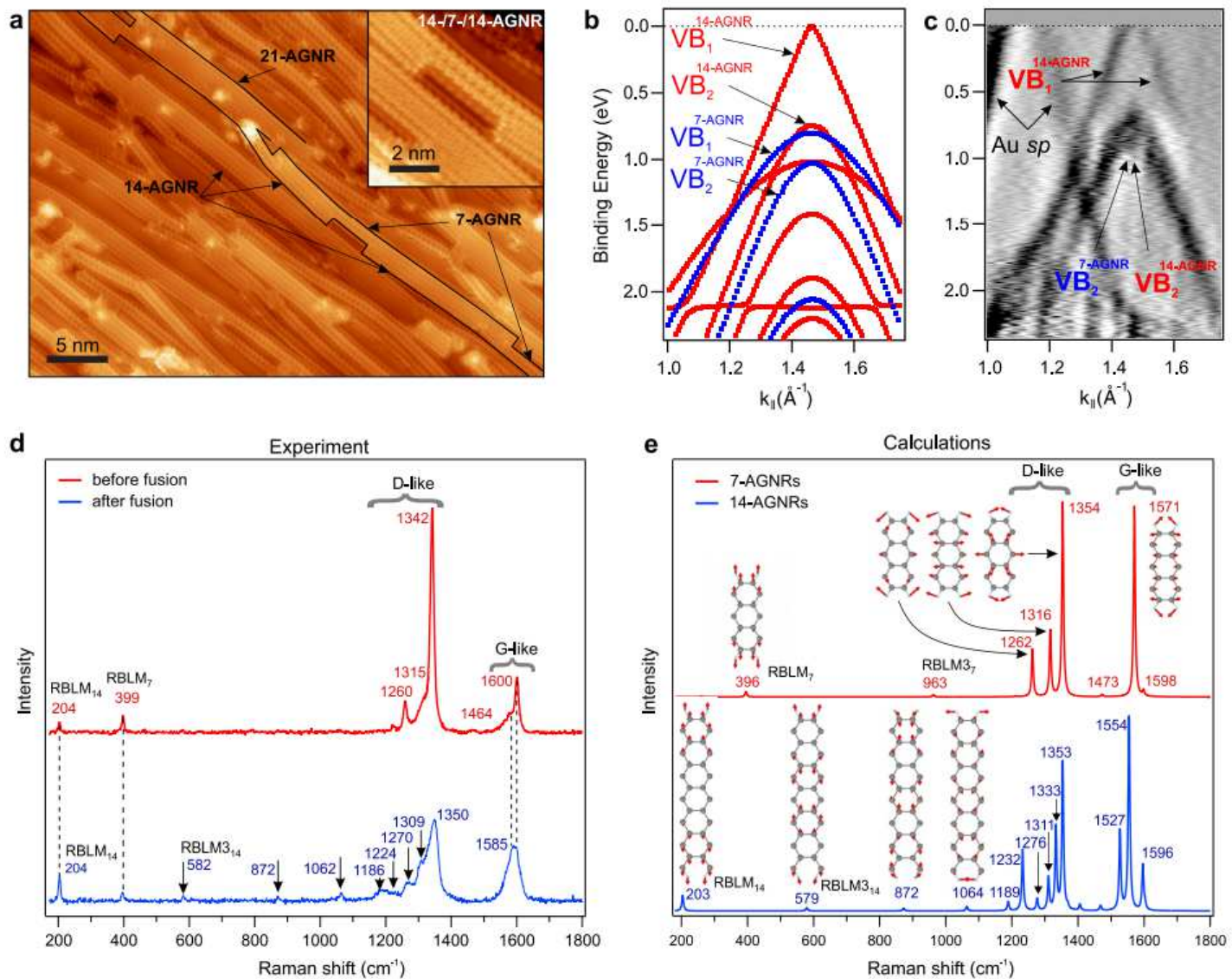


Figure 2

Experimental characterization of GNR heterojunctions on Au(788). (a) STM topographic image of fused 7-AGNRs (sample bias $V_s = -1.3$ V, tunneling current $I_t = 1.8$ nA). The black lines outline one possible conducting path through the GNR heterojunctions: quasi-metallic 14- and 21-AGNRs connected by 7-AGNR segments. The inset shows an example of a typical 14-/7-/14-AGNR heterojunction with a short (≈ 3 nm) 7-AGNR segment. See also Supplementary Section 1. (b) Calculated electronic band structure of 7-AGNRs (blue) and 14-AGNRs (red) shown in the second Brillouin zone of GNRs, where the ARPES scans were acquired. The valence band maxima in the calculations are aligned to the ARPES data. (c) Second derivative with respect to momentum of the ARPES scan (to enhance the contrast) of fused GNRs on Au(788) measured along the GNR axis (k_{\parallel}) with fixed in-plane momentum perpendicular to the axis (k_{\perp}). To maximize the photoemission intensity from VB1 14-AGNR, we used $k_{\perp} = 1.1 \text{ \AA}^{-1}$. At this k_{\perp} the intensities from VB2 14-AGNR and VB2 7-AGNR overlap (Supplementary Section 2). The Au sp bands that are from the substrate are also indicated. (d) UHV Raman spectra (300 K, 633 nm) of GNRs on Au(788) before and after fusion. The frequencies of the respective Raman peaks are indicated (values in cm^{-1}).

(e) Calculated Raman spectra of 7- and 14-AGNR. Eigenvectors of selected phonon modes are shown (Supplementary Section 4). The RBLM37 and RBLM314 are the third overtones of RBLM7 and RBLM14, respectively.

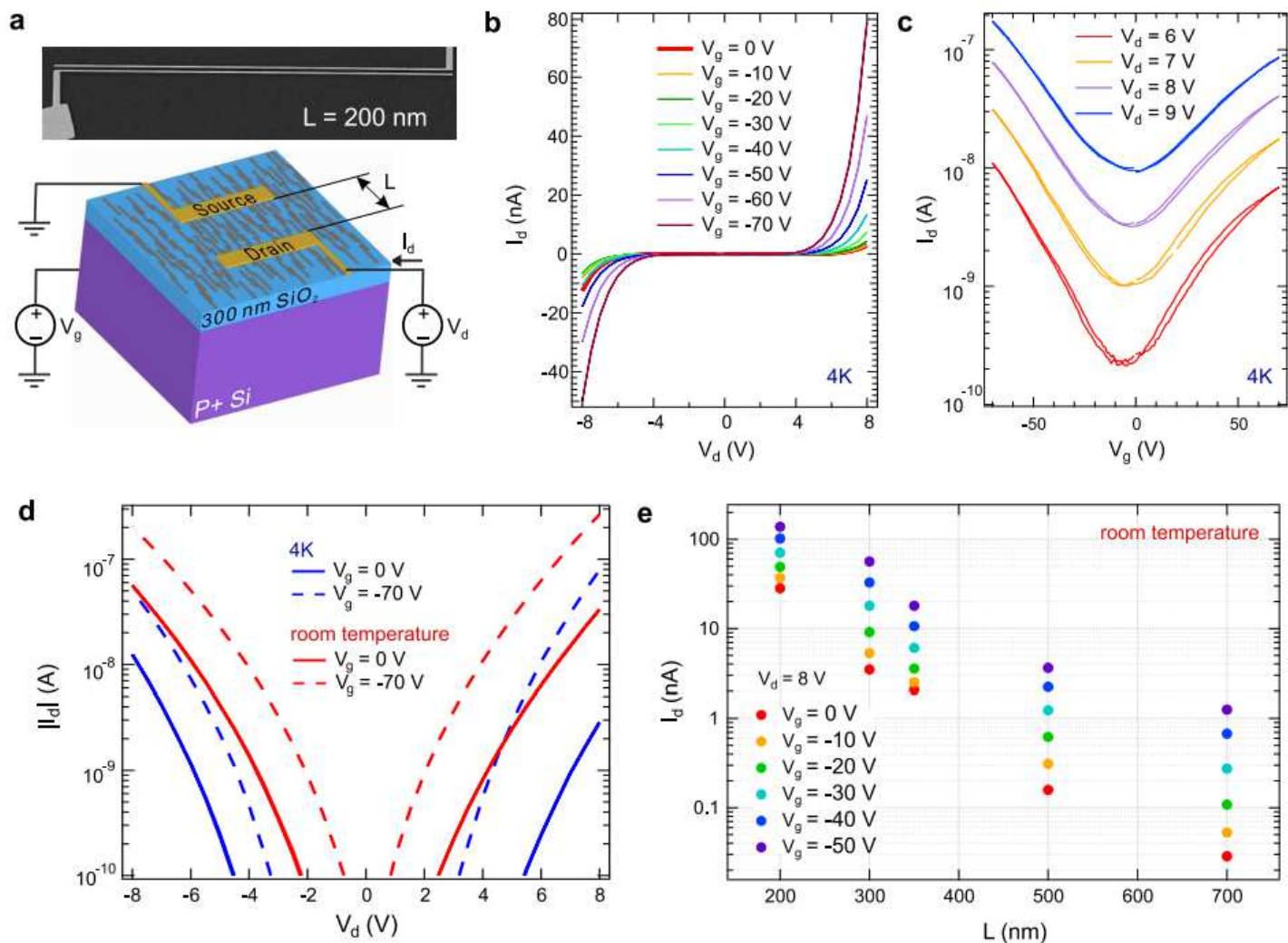


Figure 3

Charge transport characterization of the transferred GNR heterojunctions. (a) Top: scanning electron microscopy image of the device with $L = 200$ nm and $W = 25$ μm . Bottom: sketch of aligned GNR heterojunctions on SiO_2/Si in a FET geometry with source, drain and gate contacts. (b-d) Transport characteristics of the device with $L = 200$ nm. (b) I_d - V_d curves at different V_g , and (c) I_d versus V_g at different V_d at 4K . (d) I_d - V_d curves in log scale at 4K (blue) and room temperature (red) at $V_g = 0$ and -70 V. (e) Channel length dependence of the I_d at $V_d = 8$ V and different V_g at room temperature.

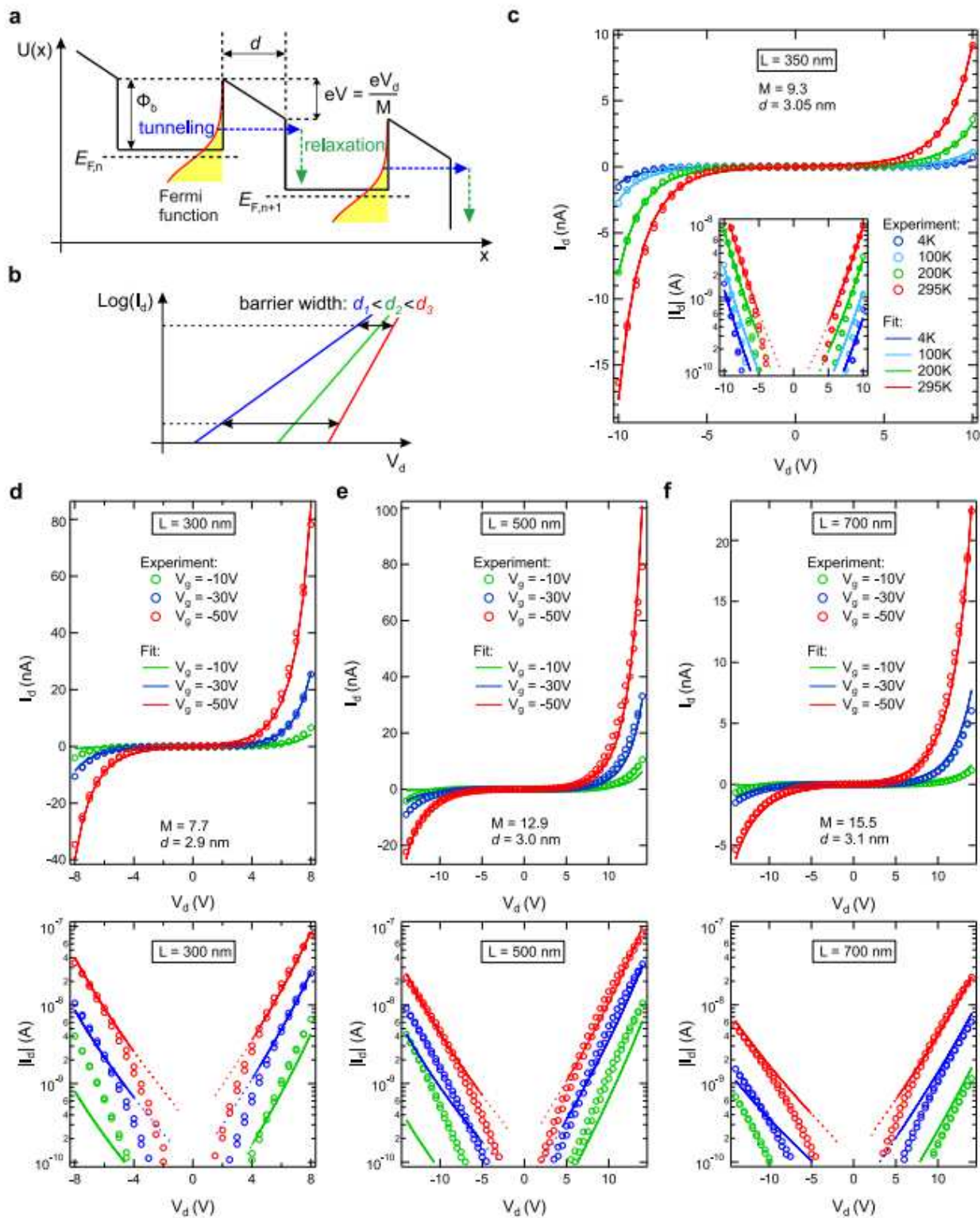


Figure 4

Comparison of experimental and calculated I_d - V_d curves. (a) The energy diagram along one conducting channel of GNR heterojunctions. The tunneling through a barrier followed by relaxation of the carrier is illustrated. The Fermi level of the n -th barrier is indicated as $E_{F,n}$. The energy drop across one barrier, equal to $eV = eV_d/M$ (where e is the electron charge and M is the number of barriers in the channel), is indicated along with the barrier height Φ_b and the barrier length d . (b) Sketch of $\text{log}(I_d)$ versus V_d

characteristics of three different barriers. At high I_d the voltage drops V_d across the barriers assume a narrower distribution (indicated by horizontal arrows). (c) Experimental and calculated I_d - V_d curves of the 350 nm channel device at different temperatures between 4 K and 295 K at $V_g = 0$. The inset shows the I_d - V_d curves in a log scale. (d-f) Experimental and calculated I_d - V_d curves for devices with $L = 300$ nm, 500 nm, and 700 nm at different V_g and at 295 K in a linear (top) and log (bottom) scales.

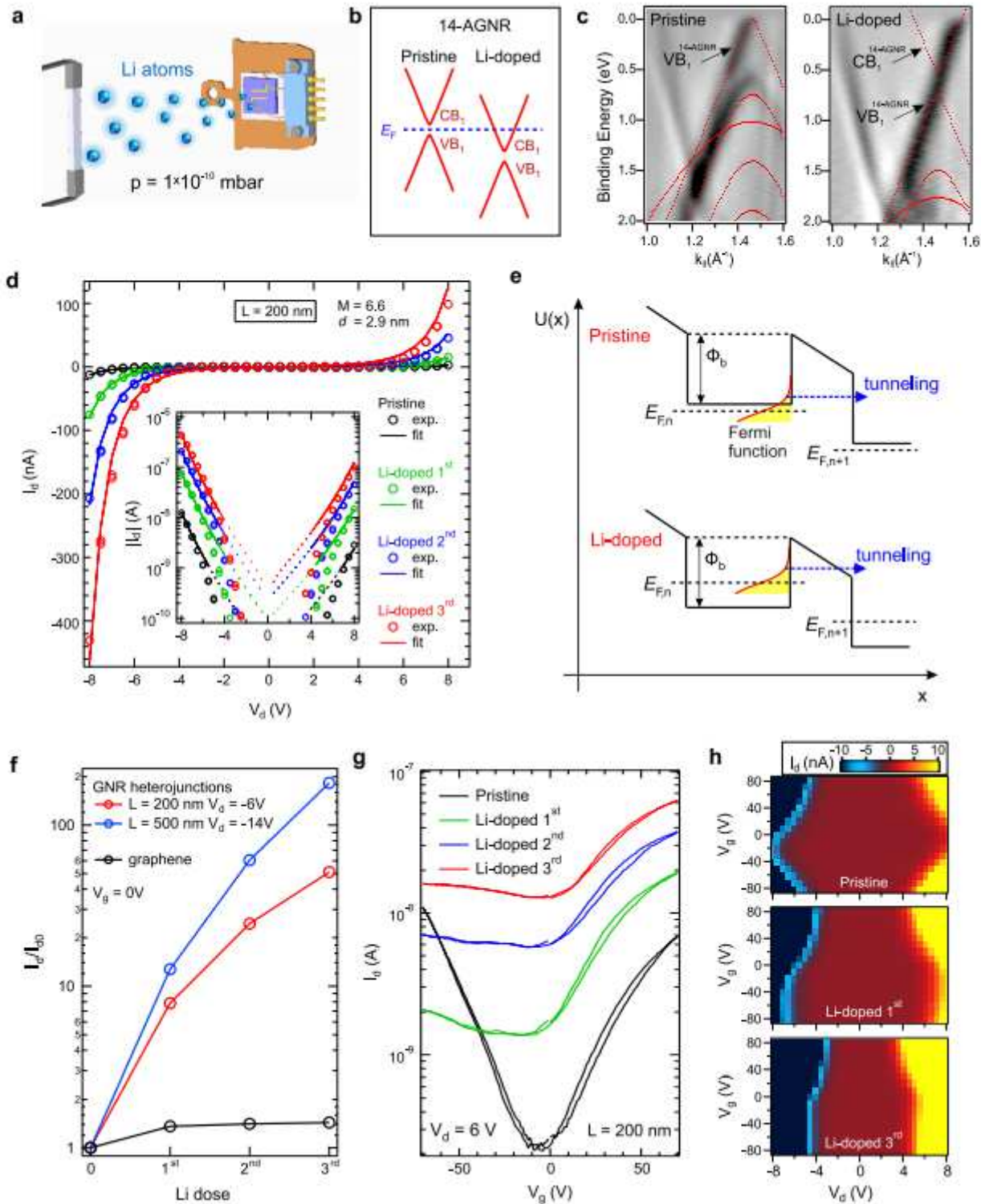


Figure 5

Band structure and charge transport of Li doped GNR heterojunctions. (a) Sketch of the experimental setup containing a Li source and the GNR heterojunction FET mounted on a UHV compatible sample holder. (b) Sketch of the band structure changes of 14-AGNRs upon Li doping. (c) Second derivatives of ARPES scans by energy of the GNR heterojunctions on Au(788) before (left) and after (right) Li deposition ($\approx 1 \text{ \AA}$) at $k_{\parallel} = 0.71 \text{ \AA}^{-1}$ (Supplementary Section 3). (d) I_d - V_d characteristics before (pristine sample) and after deposition of three identical Li doses ($\approx 0.1 \text{ \AA}$ each) in linear and log (inset) scales for the $L = 200 \text{ nm}$ device. Experimental points (exp.) are shown by circles, the fit is indicated by solid lines. (e) Schematic illustration of the potential profile $U(x)$ across a tunneling barrier for pristine and Li doped GNR heterojunctions. (f) The ratio (log scale) of current after Li doping I_d to the current in pristine sample I_{d0} for three Li doses for the $L = 200 \text{ nm}$ device at $V_d = -6 \text{ V}$, for the $L = 500 \text{ nm}$ device at $V_d = -14 \text{ V}$, and for the graphene FET (Supplementary Section 7), all at $V_g = 0 \text{ V}$. (g) I_d - V_g characteristics of the $L = 200 \text{ nm}$ device at $V_d = 6 \text{ V}$ for three Li doses. (h) Color maps of the dependence of I_d on V_g and V_d for pristine and Li doped $L = 200 \text{ nm}$ device. All transport measurements were performed at 4 K .

Supplementary Files

This is a list of supplementary files associated with this preprint. Click to download.

- [GNRheterojunctionsSupplementary.pdf](#)